

## Insights into the Long-Term Flaring Events of Blazar PKS 0805-07: A Multi-Wavelength Analysis over the 2009-2023 Period

SIKANDAR A. DAR,<sup>1</sup> ZAHIR SHAH,<sup>2</sup> RANJEEV MISRA,<sup>3</sup> AND NASEER IQBAL\*

<sup>1</sup>*Department of Physics, University of Kashmir, Srinagar 190006, India.*

<sup>2</sup>*Department of Physics, Central University of Kashmir, Ganderbal 191201, India.*

<sup>3</sup>*Inter-University Center for Astronomy and Astrophysics, Post Bag 4, Ganeshkhind, Pune, 411007 India.*

### ABSTRACT

We conducted a comprehensive temporal and spectral study of the FSRQ PKS 0805-07 by using the broadband observations from the Fermi-LAT and Swift-XRT/UVOT instruments over the period MJD 54684-60264. The 3-day binned  $\gamma$ -ray light curve during the active state, revealed eleven distinct peak structures with the maximum integral flux ( $E > 100$  MeV) reached  $(1.56 \pm 0.16) \times 10^{-6}$  photons  $\text{cm}^{-2} \text{s}^{-1}$  on MJD 59904.5. The shortest observed  $\gamma$ -ray variability was  $2.80 \pm 0.77$  days. A correlation analysis between the  $\gamma$ -ray spectral index and flux indicated the typical trend of hardening when the source is brighter, commonly observed in blazars. We identified a lag of 121 (+27.21, -3.51) days in the spectral index relative to the flux, within the time interval MJD 59582 to 60112. The Anderson-Darling test and histogram-fit rejected the normality of the  $\gamma$ -ray flux distribution, and instead suggest a log-normal distribution. To gain insight into the underlying physical processes, we extracted broadband spectra from different time periods in the light curve. The spectral energy distribution during various flux states were well-reproduced using synchrotron, synchrotron-self-Compton, and external-Compton emissions from a broken power-law electron distribution. The seed photons required for the external Compton process are from IR region. A comparison of the best-fit physical parameters indicated that the variations in different flux states were primarily associated with an increase in the bulk Lorentz factor and magnetic field from low to high flux states.

*Keywords:* radiation mechanisms: non-thermal - galaxies: active - galaxies: individual: PKS 0805-07 - gamma-rays: galaxies.

### 1. INTRODUCTION

PKS 0805-07 is a flat-spectrum radio quasar (FSRQ), located at a high redshift  $z = 1.837$  (White et al. 1988). FSRQ is a subclass of most distinctive and powerful Active Galactic Nuclei (AGNs) called Blazars. The majority of extra-galactic entities observed in the  $\gamma$ -ray sky, as detected by instruments like the Fermi Gamma-ray Space Telescope (Abdo et al. 2010a), are represented by blazars. Blazars exhibits exceptional observational properties which are attributed to the presence of a powerful non-thermal relativistic jet of plasma pointing toward the observer, originating from the vicinity of a central supermassive black hole (Urry & Padovani

1995). These include rapid flux and spectrum variability across all wavelength bands with timescales ranging from a few minutes to years, high and variable polarization, high energetic gamma-ray emissions and apparent superluminal motion as documented in numerous studies (e.g., Aharonian et al. (2007); Ackermann et al. (2016); Villata et al. (2006); Fan et al. (2021); Xiao et al. (2022); Tripathi et al. (2023); Di Gesu et al. (2022); Jorstad et al. (2022); Fan et al. (2011); Qian (2023)).

PKS 0805-07 is listed in the Fermi 4FGL catalog under the identifier 4FGL J0808.2-0751 (Abdollahi et al. 2020). This source is well known for its exceptionally high apparent jet motions (Lister et al. 2019). The active state of the source has been consistently reported in multiple astronomical telegrams (e.g. references). Ciprini (2009a) reported a high state with a  $\gamma$ -ray flux ( $E > 100$  MeV) of  $1.60 \pm 0.33 \times 10^{-6}$  photons  $\text{cm}^{-2} \text{s}^{-1}$

\* Department of Physics, University of Kashmir, Srinagar 190006, India.

on July 22, 2009, almost a factor of 2 higher than the flux reported by Ciprini (2009b). On October 11, 2022, this source displayed an elevated state of  $\gamma$ -ray emissions, with a daily averaged flux ( $E > 100 \text{ MeV}$ ) of approximately  $(1.4 \pm 0.2) \times 110^{-6} \text{ photons cm}^{-2} \text{ s}^{-1}$ . This marks a 16-fold increase compared to the average flux reported in the third release of the Fourth Fermi-LAT catalog (Abdollahi et al. 2022). The corresponding photon index was approximately  $1.97 \pm 0.09$ , notably lower than the 4FGL-DR3 value of  $2.23 \pm 0.01$ . The spectral hardening persisted on October 12, 2022, with the source detected at a flux of approximately  $(1.2 \pm 0.2) \times 10^{-6} \text{ photons cm}^{-2} \text{ s}^{-1}$  and a spectral index of approximately  $1.98 \pm 0.10$  (La Mura 2022). This event represented the second most significant  $\gamma$ -ray flare observed by LAT from this source, following the flux reported on July 22, 2009 Ciprini (2009a).

The Australia Telescope Compact Array (ATCA) has been observing PKS 0805-07 across multiple frequencies, ranging from 2.1 GHz to 45 GHz, since 2006. The majority of these observations were conducted as part of the Observatory-led Active Galactic Nuclei (AGN) monitoring program (C007). The latest measurements are derived from the TANAMI/C1730 program, targeting  $\gamma$ -ray bright blazars in the southern sky. In addition, PKS 0805-07 has been part of the Metsahovi AGN monitoring program since mid-2002, and from 2009 onward, it has been consistently monitored at 37 GHz with a high cadence.

Starting in early 2021, the high-frequency emission from PKS 0805-07 has shown a significant increase above its long-term average state. The most recent measurements, recorded on September 25, 2021, and October 12, 2021 indicate historically high flux densities for this source, with values of  $4.0 \pm 0.2 \text{ Jy}$  and  $4.1 \pm 0.2 \text{ Jy}$ , respectively, in both the ATCA and Metsahovi monitoring programs (Edwards et al. 2022). Furthermore, the GRID detector on the AGILE satellite has detected a prominent  $\gamma$ -ray flare from PKS 0805-07. A preliminary multi-source likelihood analysis indicates a 6 sigma detection, with a  $\gamma$ -ray flux ( $F(>100 \text{ MeV})$ ) of  $(2.7 \pm 0.8) \times 10^{-6} \text{ photons cm}^{-2} \text{ s}^{-1}$  during the period of November 17-19, 2022 (Bulgarelli et al. 2022). This marks a substantial increase compared to the average flux observed in the preceding seven days.

The spectral energy distribution (SED) of blazars typically displays a distinctive double-peaked pattern. The theoretical models used to interpret the observed broadband SED of blazars mainly fall into two categories: leptonic and hadronic origins. The low-energy component, peaking at optical/UV/X-ray energies, is attributed

to Doppler-boosted synchrotron emission. The high-energy component, peaking in the  $\gamma$ -ray range, is often explained by leptonic process via Inverse Compton (IC; Böttcher et al. (2013); Shah et al. (2017)) and hadronic emission processes through the proton-synchrotron process or proton-photon interactions (Mücke et al. 2003; Mücke & Protheroe 2001; Mannheim 1993). These interactions can give rise to  $\gamma$ -ray photons and high-energy neutrinos. Inverse Compton (IC) involves primarily two processes. One is synchrotron self Compton (SSC), where relativistic particles in the jet cause the up-scattering of synchrotron photons (Jones et al. 1974; Maraschi et al. 1992; Ghisellini et al. 1993). Another is the external Compton (EC) process, where relativistic particles in the jet up-scatter photons external to the jet (Dermer et al. 1992; Sikora et al. 1994; Błażejowski et al. 2000; Shah et al. 2017).

In a recent study conducted by Prokhorov & Moraghan (2017), the authors identified indications of periodic behaviors in four blazars: 4C + 01.28, S5 0716+71, PKS 0805-07, and PKS 2052-47 apart from the previously asserted quasi-periodic  $\gamma$ -ray blazars. Among these, three sources including PKS 0805-07 are situated at elevated redshifts and emerge as potential candidates for binary systems of supermassive black holes (SMBHs).

The identification of neutrino events from blazars TXS 0506+056 associated with the high-energy neutrino IC-170922A (IceCube Collaboration et al. 2018), has sparked increased interest in hybrid models, particularly lepto-hadronic models. These models aim to enhance our understanding of the broadband Spectral Energy Distribution (SED) of blazars (Ansoldi et al. 2018; Sahakyan 2018; Gasparyan et al. 2022; Keivani et al. 2018).

Despite the extensive list of high-flux detections, a comprehensive long-term investigation of the source has been lacking until now. Our study is the first to conduct comprehensive broadband temporal and spectral analyses of PKS 0805-07 using multi-wavelength observations from Fermi-LAT and Swift-XRT/UVOT. This allows us to examine its variability in unprecedented detail. Additionally, the motivation for studying PKS 0805-07 lies in its potential to serve as a case study for testing the theoretical models. In our work, we used the broadband observations of the source in different flux states, to check the consistency of our convolved one zone leptonic model. The model is incorporated as local convolution model in XSPEC and outputs broadband spectrum for any input particle distribution. This model is tested previously for the BL Lac source (Shah 2024). Our work aims to highlight the importance of individual case studies in astrophysics, demonstrating the im-

portance of continuous observation and analysis of individual blazars, as even well-studied objects can reveal important features under different observational conditions. The structure of this paper is as follows: Section §2 provides details on the multi-wavelength data and the procedures for data analysis, while Section §3 presents the broadband spectral and temporal findings of the source. The concluding section, §4, summarizes and discusses the results.

## 2. OBSERVATIONS AND DATA REDUCTION

### 2.1. *Fermi-LAT*

Fermi-LAT is a high-energy space-based telescope aboard the Fermi Gamma-ray Space Telescope (previously GLAST). It was launched by NASA in 2008 and has a wide field of view of approximately 2.3 Sr. Operating primarily in scanning mode, it surveys the entire sky in the energy range of about 20 MeV to 500 GeV every three hours (Atwood et al. 2009). This study focused on retrieving  $\gamma$ -ray data from Fermi-LAT for PKS 0805-07 during the time period MJD 54684–60264. For temporal and spectral analysis, the data were processed using FermiTools (formerly Science Tools) version 2.2.0, available on an Anaconda Cloud channel maintained by the Fermi Science Support Center (FSSC). Standard analysis procedures outlined in the Fermi-LAT documentation were followed for data reduction<sup>1</sup>. P8R3 events were extracted from a 15-degree region of interest centered at the source location, with a focus on including high-probability photon events of the SOURCE class (evclass=128, evttype=3). To mitigate background  $\gamma$ -rays from the Earth limb, a zenith angle cut of 90 degrees was applied to the data. In the spectral analysis, we focused on photons within the energy range of 0.1–300 GeV. Additionally, we utilised FERMIPY, v1.0.1 Wood et al. (2017), for the analysis. The galactic diffuse emission component was characterised using the *gll\_iem\_v07.fits* model, and the isotropic emission component was represented by *iso\_P8R3\_SOURCE\_V3\_v1.txt*. Our work employed the post-launch instrument response function *P8R3\_SOURCE\_V3*. All the sources located within a 25 degree region of interest (ROI) centered on the source position in the 4FGL catalog were incorporated into the XML model file. For the spectral analysis, we kept the normalisation of the sources lying within 10 degree of ROI as free parameters. In addition to normalisation, the spectral parameters (alpha and beta) of PKS 0805-07 were also kept free. All other parameters of the sources were kept frozen to their 4FGL catalog

value. We generated SED's for various activity periods. We generated 3-day, 7-day, 15-day, 1-month, 3-month, and 6-month binned  $\gamma$ -ray light curves for the temporal study.

### 2.2. *Swift-XRT*

The X-ray data utilized in this study were acquired through the Swift-XRT instrument aboard the Neil Gehrels Swift Observatory (Gehrels et al. 2004). The Swift-XRT light curve was derived, with each observation ID corresponding to a distinct point in the X-ray light curve. To process the X-ray data collected in photon-counting mode, we utilized the XRTDAS V3.0.0 software package, which is an integral part of the HEASoft package (version 6.29). Following the guidelines provided in the Swift analysis thread page, we used the standard XRTPIPELINE (version: 0.13.6) to generate level 2 cleaned event files. Source events for spectral analysis were selected from a circular region with a radius of 50 arcsec, while the background spectra were selected from a circular region with a radius of 100 arcsec outside the source region. The XIMAGE tool was employed to integrate exposure maps, and the xrtmkarf task was utilized to generate auxiliary response files. Using the GRPPHA task, source spectra were binned to ensure that each bin contained a minimum of 20 counts. For the spectral analysis, XSPEC version 12.12.0 was employed (Arnaud 1996). In order to account for the absorption effects due to neutral hydrogen, we used the Tbabs model. The neutral hydrogen column density (nH) value were fixed at a constant value of  $9.60 \times 10^{20} \text{ cm}^{-2}$  (Kalberla et al. 2005).

### 2.3. *Swift-UVOT*

Besides the X-ray information, Swift also gives us data in the Optical/UV range using the Swift-UVOT telescope (Roming et al. 2005). This telescope observes in optical and UV using different filters like v, b, u, w1, m2, and w2 (Poole et al. 2008; Breeveld et al. 2010). We obtained the PKS 0805-07 data from the HEASARC Archive. We used the HEASoft package (v6.29) to extract useful scientific products from the data. To process the images, we used a package called uvotsource from the HEASoft package (v6.26.1). We added multiple images taken with different filters using the uvotimsum tool. We extracted the source counts by focusing on a circular area with a radius of 5'' centered at the source location. The background region was taken from a nearby source free circular area of radius of 10''. To make our observations more accurate, we adjusted for the impact of dust in our galaxy. This involved correcting for Galactic ex-

<sup>1</sup> <http://fermi.gsfc.nasa.gov/ssc/data/analysis/>

inction using specific values  $E(B - V) = 0.3711$  and  $R_V = A_V/E(B - V) = 3.1$  (Fitzpatrick & Massa 2007).

### 3. RESULTS

#### 3.1. Temporal Analysis

To explore the temporal behavior of the source, we generated 3-day, 7-day, 15-day, 1-month, 3-month, and 6-month binned long-term  $\gamma$ -ray light curves. For the temporal analysis, we retained the time bins which have detection significance ( $TS \geq 4$ ). The flux in the light curves are integrated over the energy range of 0.1–100 GeV. This dataset spans the period from MJD 54684 to 60264. The Table 1 presents the maximum  $\gamma$ -ray flux, along with the associated spectral index, time and TS value, for various time-binned  $\gamma$ -ray light curves.

To identify flaring episodes, we followed the approach outlined in Meyer et al. (2019). In this approach, the Bayesian Block method (BB, Scargle et al. 2013) is combined with the HOP algorithm (HOP, Eisenstein & Hut 1998) to segment a light curve into groups that distinguish between quiescent and flaring episodes. The HOP group is the segment of light curve where the multiple consecutive BBs are connected. In Figure 1, we have shown the variation of 7-day binned flux values and the corresponding index values with respect to the time. We have designated HOP 8 (MJD 59370–59965) as the “active state” of the source. The average flux in this time period is higher than the average flux between MJD 54684–59370 (see Table 1). Figure 1 suggests a negative correlation between the flux and index. To validate this observation, we plotted the spectral index against the 7-day binned  $\gamma$ -ray flux, applying the condition that the flux/flux-error > 3. The yellow solid circles in Figure 2 represent the individual flux-index pairs. Since the lower flux values are associated with larger index errors, we refined the analysis by creating a gamma-ray light curve with time bins corresponding to the BBs derived from the 7-day binned light curve. The flux and index values obtained for each block are also plotted in Figure 2, represented by black solid circles. The results indicate that the source demonstrates a mild “harder when brighter” trend, a common phenomenon observed in blazars (Hota et al. 2021; Shah et al. 2019). Applying the Spearman rank correlation method, we obtained a correlation coefficient of  $-0.25$  with a null-hypothesis probability of  $2.62 \times 10^{-5}$  for individual flux-index pairs, and a correlation coefficient of  $-0.50$  with a null-hypothesis probability of  $6.80 \times 10^{-4}$  for the BB analysis. These results further indicate the mild anti-correlation between the index and flux values. However, in previous studies e.g., Hota et al. (2021); Shah et al. (2019), a clear harder-when-

brighter behavior is observed during specific flaring periods. It is important to note here that the full 7-day binned dataset includes various flux states of the source, ranging from low to high. Therefore, when analyzing the entire data sample, different physical mechanisms may dominate at different flux levels, potentially masking a more obvious correlation. Additionally, the uncertainties related to low-flux states are not considered in the Spearman correlation, so the obtained results should be interpreted with caution. Further, the flux and index light curves (see Figure 1) shows a possible lag between the index and flux. Therefore to confirm the lag, we utilized the Z-transformed discrete correlation function (ZDCF, Alexander 1997) to find the possible lag between flux and index in the time interval MJD 59582–60112 using 3-day binned  $\gamma$ -ray light curve. We found the index lagging behind the flux by 121 days (+27.2, -3.51). The uncertainties are at  $1 \sigma$  confidence level.

The  $\gamma$ -ray light curve displays notable variations with number of low and high flaring components. To undertake a detailed temporal analysis of the source, we chose the ‘active state’ of the source (see Figure 1). During this time, both the 3-day and 7-day binned  $\gamma$ -ray light curves exhibit a peak in integral flux. We determined the rise and decay times for these components in this ‘active state’ using the sum of exponential (SOE) function (Abdo et al. 2010b):

$$F(t) = F_b + \sum F_i(t), \quad (1)$$

where  $F_b$  represents the baseline flux, and

$$F_i(t) = \frac{2F_{p,i}}{\exp\left(\frac{t_{p,i}-t}{\tau_{r,i}}\right) + \exp\left(\frac{t-t_{p,i}}{\tau_{d,i}}\right)}, \quad (2)$$

In this equation,  $F_{p,i}$  is the peak flare amplitude at time  $t_{p,i}$ , while  $\tau_{r,i}$  and  $\tau_{d,i}$  denote the rise and decay times of the respective flare component. The fitted SOE profile along with the 3-day binned  $\gamma$ -ray light curve, are shown in Figure 3.

We used 11 exponentials in the SOE function, yielding a  $\chi^2/\text{dof}$  value of 123.64/129. Table 2 provides the best fit parameters for components for which the ratio of parameter value and its error > 2. Using rise/decay time scales, we determined the profile shapes of these components by calculating the parameter,  $\zeta = \frac{\tau_d - \tau_r}{\tau_d + \tau_r}$ , such that the component is symmetric if  $|\zeta| < 0.3$ , moderately asymmetric if  $0.3 < |\zeta| < 0.7$ , and asymmetric if  $0.7 < |\zeta| < 1$  (Abdo et al. 2010b). We noted that

**Table 1.** Col. 1: denotes the time bin, 2: denotes the time (MJD) corresponding to maximum flux, 3: represents the maximum flux (measured in units of  $10^{-6}$  photons  $\text{cm}^{-2} \text{s}^{-1}$ ), 4 and 5: display the spectral index and TS Value, 6 and 7: represent the averaged flux ( $F_{av}$ , in units of  $10^{-7}$  photons  $\text{cm}^{-2} \text{s}^{-1}$ ) between MJD 54684–59370 and MJD 59370–59965, respectively.

Time Bin	Time	Flux	Index	TS	$F_{av}$ (54684–59370)	$F_{av}$ (59370–59965)
3-day	59904.49	$1.56 \pm 0.16$	$2.13 \pm 0.08$	456.63	$0.49 \pm 0.01$	$2.10 \pm 0.05$
7-day	59901.49	$1.34 \pm 0.11$	$2.13 \pm 0.07$	802.74	$0.34 \pm 0.01$	$2.50 \pm 0.05$
15-day	59907.49	$0.83 \pm 0.05$	$2.08 \pm 0.05$	1355.88	$0.63 \pm 0.02$	$2.64 \pm 0.06$
1-month	59854.99	$0.63 \pm 0.03$	$1.95 \pm 0.04$	2792.13	$0.68 \pm 0.02$	$3.22 \pm 0.06$
3-month	59884.99	$0.53 \pm 0.02$	$2.07 \pm 0.02$	5729.90	$0.65 \pm 0.02$	$3.36 \pm 0.07$
6-month	59839.99	$0.52 \pm 0.01$	$2.05 \pm 0.02$	10315.86	$0.68 \pm 0.02$	$3.43 \pm 0.08$

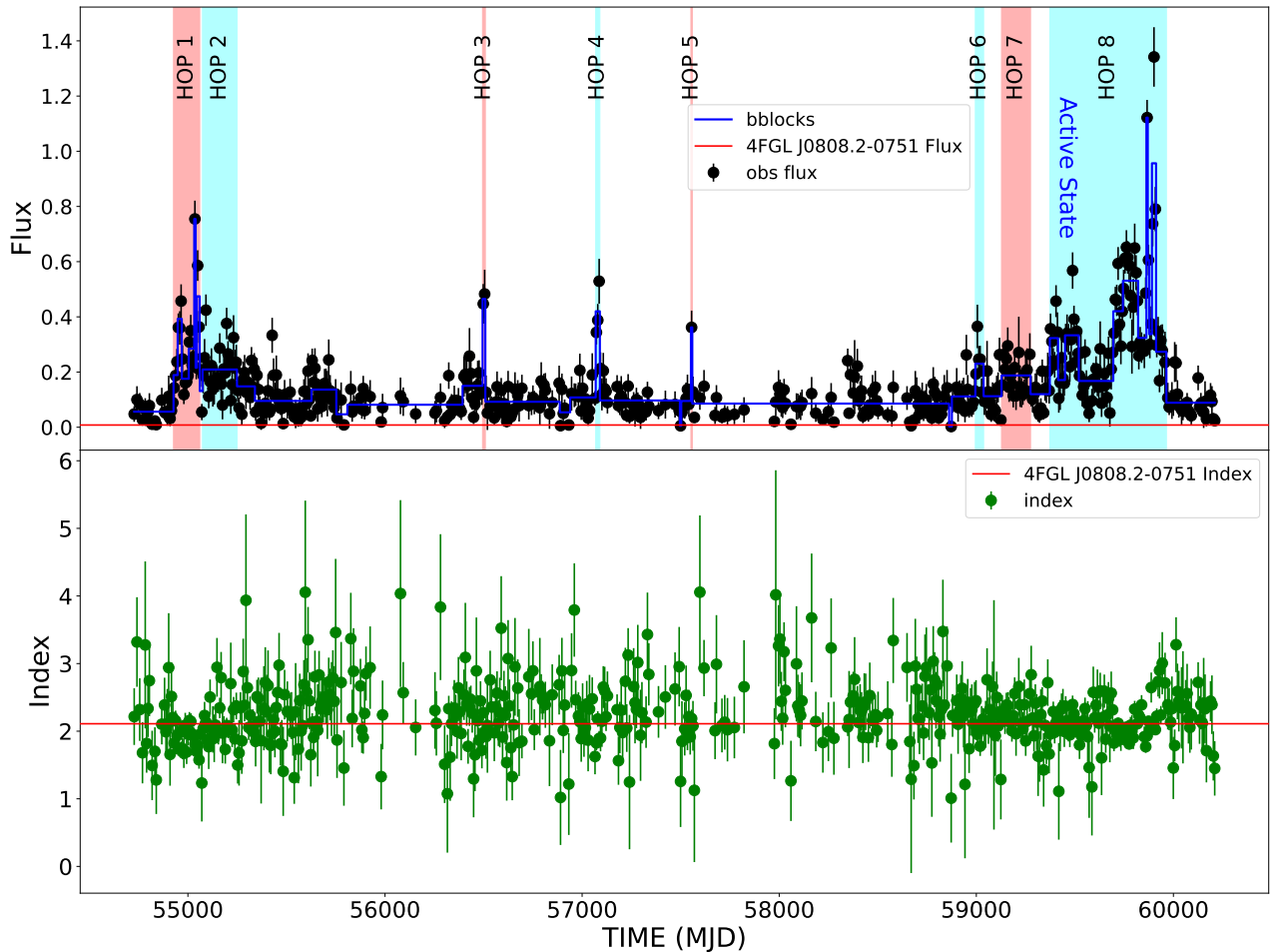


**Figure 1.** The upper panel depicts the 7-day binned  $\gamma$ -ray light curve of PKS 0805-07, integrated over the energy range of 0.1–100 GeV [Flux ( $E > 100$  MeV)] in units of  $10^{-6}$  photons  $\text{cm}^{-2} \text{s}^{-1}$  from MJD 54684 to 60264. The lower panel showcases the corresponding values of spectral index for the source during the same period. The red horizontal lines in the upper and lower panel represent the flux and index reported in the 4FGL catalog, respectively. The shaded regions represents the HOPs and HOP 8 is designated as “active state”. The different colors representing HOPs are solely for demarcation purposes.



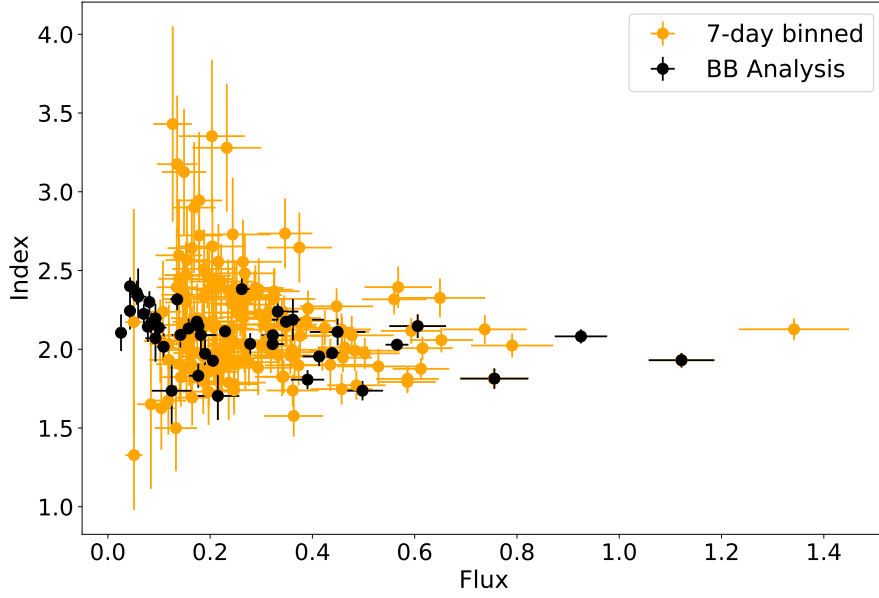


**Figure 2.** Correlation plot between index and flux in 7-day binned light curve. The yellow solid circles represent the individual flux-index pairs and the black solid circles represent the flux-index pairs based on BB analysis. Flux is measured in units of  $10^{-6}$  photons  $\text{cm}^{-2} \text{s}^{-1}$ .

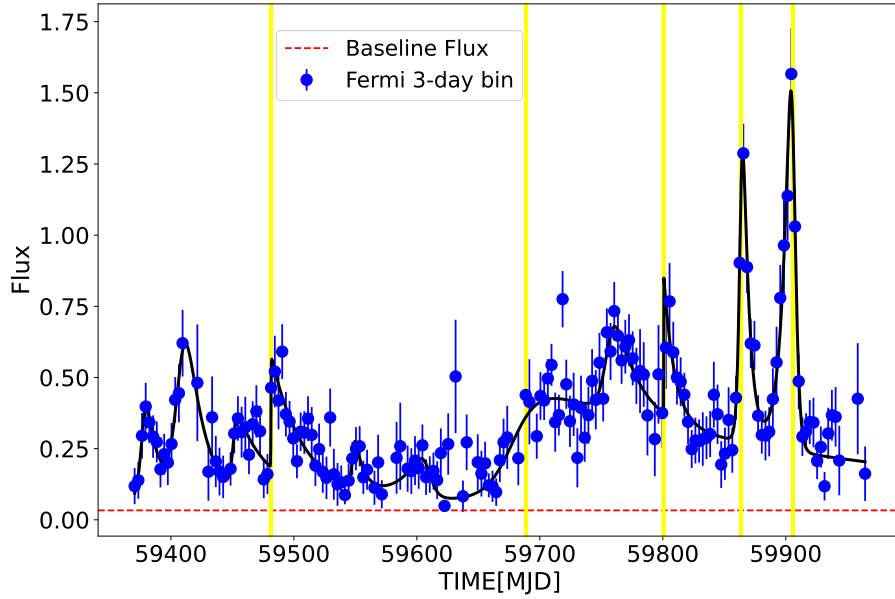


**Figure 3.** 3-day binned  $\gamma$ -ray light curve of PKS 0805-07 fitted with the SOE function defined in Equation 1. Yellow strips denotes the peak time (MJD) of the significant peaks as mentioned in Table 2. The horizontal red line denotes the baseline flux. Flux is measured in units of in units of  $10^{-6}$  photons  $\text{cm}^{-2} \text{s}^{-1}$ .

two components are moderately asymmetric and three components are asymmetric.

To estimate the shortest timespan for the doubling of flux, we examined the 3-day binned  $\gamma$ -ray light curve using the equation:

$$F(t) = F(t_0) \times 2^{\frac{t-t_0}{\tau}}, \quad (3)$$

here,  $F(t_0)$  and  $F(t)$  represent the flux values at times  $t_0$  and  $t$  respectively, and  $\tau$  denotes the characteristic doubling time scale. By using the condition that the difference in flux at times  $t$  and  $t_0$  is significant at a level of  $(3\sigma)$  or greater (Foschini et al. 2011), we identified the shortest time variability as  $(2.80 \pm 0.77)$  days.

### 3.2. Flux Distribution

The examination of flux distribution of astrophysical systems serves as a valuable tool for investigating the underlying physical processes contributing to variability. For instance, the presence of a normal flux distribution suggests additive processes, while a lognormal distribution indicates multiplicative processes. Typically, the observed flux distribution in compact black hole systems follows a lognormal distribution. To explore this, we characterize the  $\gamma$ -ray flux distribution of the source by conducting Anderson-Darling (AD) and histogram fitting tests. The AD test produces a test statistic (TS) value of 13.30, which is well above the critical value (CV) of 0.76 at the 5% significance level. Thus AD test rejects the normality of the flux distribution. However, the AD test supports the lognormality of the flux distribution, with a statistic value of 0.54 for the log of the flux distribution, which is smaller than the CV of 0.55 at the 15% significance level, suggesting that the null hypothesis of log-normality cannot be rejected. We additionally examined the probability density function (PDF) of the flux distribution by constructing a normalized histogram of the logarithm of flux.

The histogram is constructed with equal points per bin and varying bin widths. For the 3-day binned light curve, there are 370 significant flux points with flux/flux-error > 3, and each bin contains 10 points. The normalized histogram points are plotted in Figure 4. The resulting histogram in log-scale is fitted by:

$$L(x) = \frac{1}{\sqrt{2\pi}\sigma_l} e^{-(x-\mu_l)^2/2\sigma_l^2} \quad (4)$$

and

$$G(x) = \frac{10^x \log(10)}{\sqrt{2\pi}\sigma_g} e^{-(10^x - \mu_g)^2/2\sigma_g^2} \quad (5)$$

where  $\mu_l$  and  $\sigma_l$  are the mean and standard deviation of the logarithmic flux distribution, and  $\mu_g$  and  $\sigma_g$  are the mean and standard deviation of the flux distribution. Equation 4 represents a lognormal fit, while Equation 5 represents a normal fit. The lower and upper panels of Figure 4 show the normalized histogram and the best lognormal/normal fit, respectively. The reduced  $\chi^2$  values obtained from fitting the flux distribution with normal and lognormal PDFs were 1.76 and 0.78, respectively, suggesting that the flux distribution is more accurately described by a lognormal distribution. Observation of a lognormal distribution in the  $\gamma$ -ray light curve implies that the underlying physical processes are likely multiplicative in nature.

### 3.3. Multiwavelength Light Curve

To comprehend the behavior of PKS 0805-07 across the optical, UV, and X-ray bands, all the observations conducted by *Swift*-XRT/UVOT during the period MJD (54684 – 60264) were taken. The corresponding X-ray and optical/UV data from these observations were analyzed following the procedures outlined in Section 2. The resulting X-ray and optical/UV light curves for PKS 0805-07 are displayed in the second and bottom panels, respectively, of the multiwavelength light curve plot (refer to Figure 5). Each data point in the X-ray and optical/UV light curves corresponds to an individual observation. The top panel illustrates the 3-day binned  $\gamma$ -ray light curve, with flux points derived by integrating over the energy range 0.1–100 GeV. The part of the  $\gamma$ -ray light curve with simultaneous X-ray and optical/UV data is zoomed in and is shown at the top of the Figure 5. The multiwavelength plot shows fluctuations in flux across various energy ranges, but since the data points in X-ray and optical/UV are few, we calculated variability only in  $\gamma$ -ray light curve by computing the fractional variability amplitude using the formula (Vaughan et al. 2003):

$$F_{\text{var}} = \sqrt{\frac{S^2 - \overline{\sigma_{\text{err}}^2}}{\overline{F}^2}}, \quad (6)$$

where  $S^2$  represents the variance,  $\overline{F}$  is the mean of flux points in the light curve, and  $\overline{\sigma_{\text{err}}^2}$  is the mean of the square of the measurement errors. The uncertainty on  $F_{\text{var}}$  is determined using the equation (Vaughan et al. 2003):

$$F_{\text{var, err}} = \sqrt{\frac{1}{2N} \left( \frac{\overline{\sigma_{\text{err}}^2}}{F_{\text{var}} \overline{F}^2} \right)^2 + \frac{1}{N} \frac{\overline{\sigma_{\text{err}}^2}}{\overline{F}^2}}, \quad (7)$$

**Table 2.** The rise and fall time of the prevailing components in the light curve. Col. 1: denotes the peak time (MJD), 2: represents the peak flux (measured in units of  $10^{-7}$  photons  $\text{cm}^{-2} \text{s}^{-1}$ ), 3 and 4: display the rise time and decay time of the components (measured in days), and 5: indicates the asymmetry parameter.

$t_p$	$F_p$	$t_r$	$t_d$	$ \zeta $
$59479.66 \pm 2.20 \times 10^{-8}$	$1.92 \pm 0.42$	$0.05 \pm 9.6 \times 10^{-7}$	$29.20 \pm 11.17$	0.99
$59688.90 \pm 5.98$	$2.13 \pm 0.30$	$11.09 \pm 4.25$	$250.48 \pm 56.62$	0.92
$59800.85 \pm 1.21 \times 10^{-9}$	$2.45 \pm 0.88$	$0.02 \pm 1.35 \times 10^{-14}$	$8.3 \pm 3.4$	0.99
$59863.57 \pm 0.77$	$8.83 \pm 1.09$	$1.57 \pm 0.52$	$4.95 \pm 1.00$	0.52
$59905.85 \pm 1.05$	$11.31 \pm 1.44$	$6.11 \pm 1.21$	$2.23 \pm 0.56$	0.46

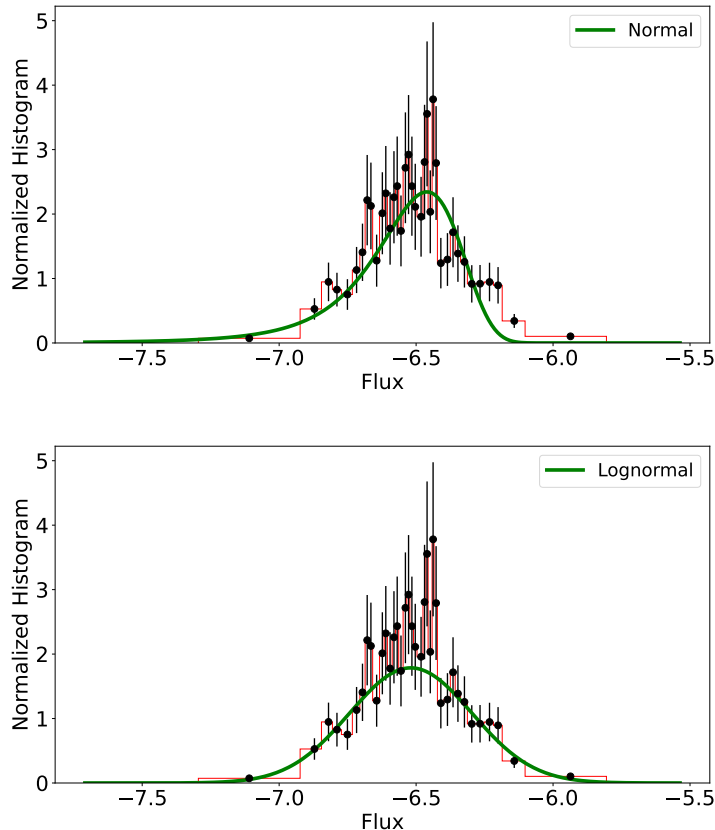


**Figure 4.** Normalized histogram of the  $\gamma$ -ray light curve. Upper panel: normalized histogram fitted using the Gaussian function. Lower panel: normalized histogram fitted using the lognormal function. Flux is measured in units of  $10^{-6}$  photons  $\text{cm}^{-2} \text{s}^{-1}$

where  $N$  is the number of points in the light curve. The  $F_{var}$  values for the  $\gamma$ -ray light curve across different time bins are shown in Figure 6, where we observed an increase in  $F_{var}$  with larger bin sizes. In our analysis, we applied a  $TS > 4$  threshold to include only statistically significant data, reducing the risk of bias from less reliable flux points. Schleicher et al. (2019) reported an opposite trend for Mrk 421, which result from including all flux points, regardless of their statistical significance. This suggests that  $F_{var}$  is highly sensitive to the data selection criteria.

### 3.4. Broadband Spectral Analysis

To understand the physical parameters responsible for simultaneous flux variations, we examine the broadband spectral characteristics of PKS 0805-07 by dividing the  $\gamma$ -ray light curve into segments using BB analysis. These segments, shown in Figure 5, represent distinct flux states (active and quiescent states). In our work, we selected the states for which the simultaneous observations are available in the X-ray and Optical/UV bands. We have illustrated these temporal intervals using vertical stripes in the multiplot (Figure 5) and categorized them



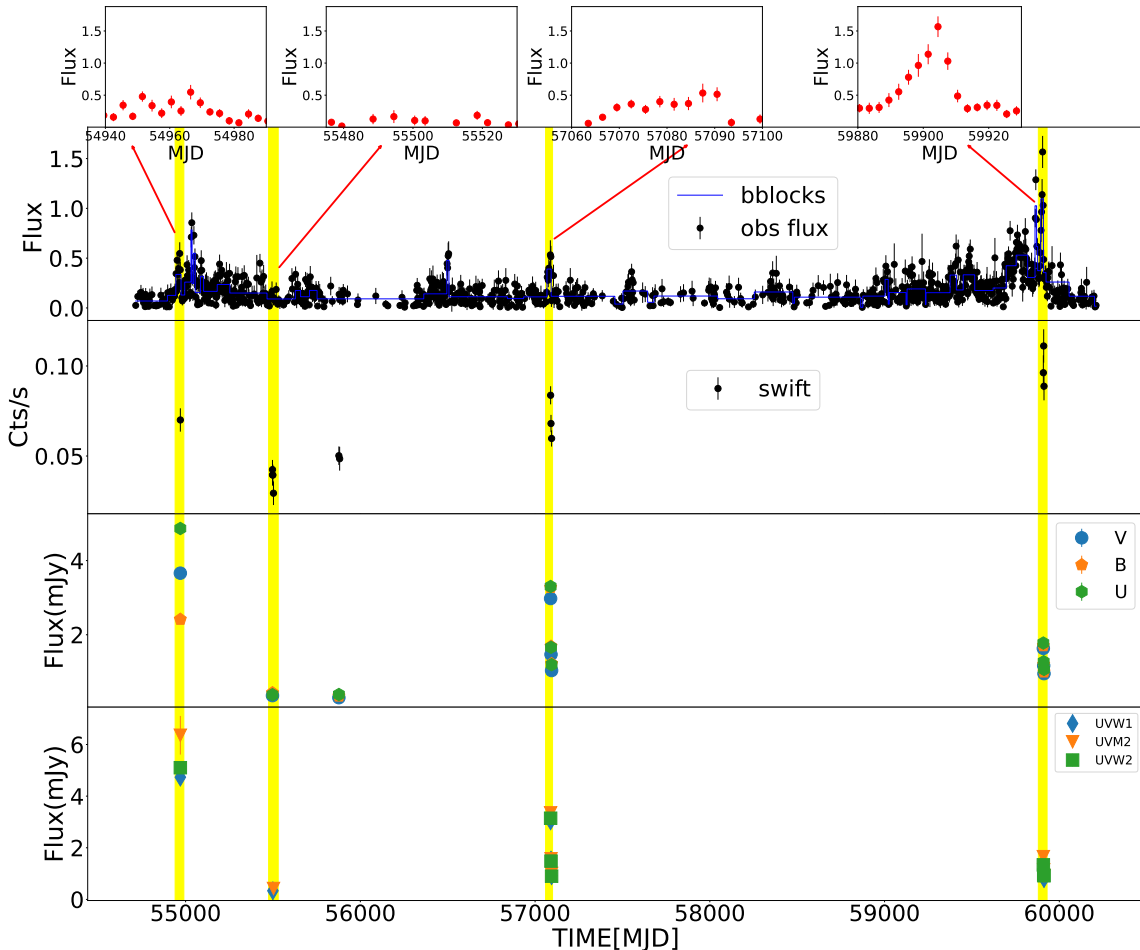


**Figure 5.** Multiwavelength light curves of PKS 0805-07 obtained using *Fermi*-LAT and *Swift* XRT and UVOT observations. The observations spanned a period from MJD 54684 to 60264. The top panel represents the 3-day binned  $\gamma$ -ray light curve (Flux is measured in units of  $10^{-6}$  photons  $\text{cm}^{-2} \text{s}^{-1}$ ), and the second, third, and fourth panels depict the X-ray, UV, and optical light curves. Colored vertical stripes indicate the regions where broadband spectral modeling is performed. The  $\gamma$ -ray light curve with simultaneous X-ray and optical/UV data is zoomed in and is shown at the top of plot, with arrows indicating their location in the multiwavelength plot.

as follows: S1 MJD 54940-54990, Q1 MJD 55475-55530, S2 MJD 57060-57100, and S3 MJD 59880-59930. S1, S2 and S3 correspond to active states, while Q1 represents a quiescent state. We characterized the  $\gamma$ -ray spectrum of the selected flux states using the log parabola (LP) model and powerlaw (PL) model. The LP and PL models are expressed as follows:

$$\frac{dN}{dE} = N_0 \frac{E^{-(\alpha+\beta \log(E/E_0))}}{E_0}, \quad (8)$$

where  $N_0$  represents the normalization,  $\alpha$  is the photon index at the scale energy,  $E_0$  is fixed at 665.74 MeV, and the parameter  $\beta$  measures the curvature in the spectrum.

$$\frac{dN}{dE} = N_0 \left( \frac{E}{E_0} \right)^{-\Gamma} \quad (9)$$

Here,  $N_0$  is the prefactor,  $\Gamma$  denotes the spectral index, and  $E_0$  is the fixed scale energy set at 733 MeV. The obtained fitting parameters are summarized in Table 3. We evaluated the statistical significance of the observed curvature in the  $\gamma$ -ray spectrum using the relation  $TS_{curve} = 2[\log \mathcal{L}(LP) - \log \mathcal{L}(PL)]$  (Nolan et al. 2012). As mentioned in Table 3, significant curvature ( $TS_{curve} > 16$ ) is observed in the S2 and S3 states.

We performed broadband spectral analysis on these segments to identify changes in physical parameters governing flux variations. We adopt a one-zone leptonic model to characterize the broadband SED during selected flux

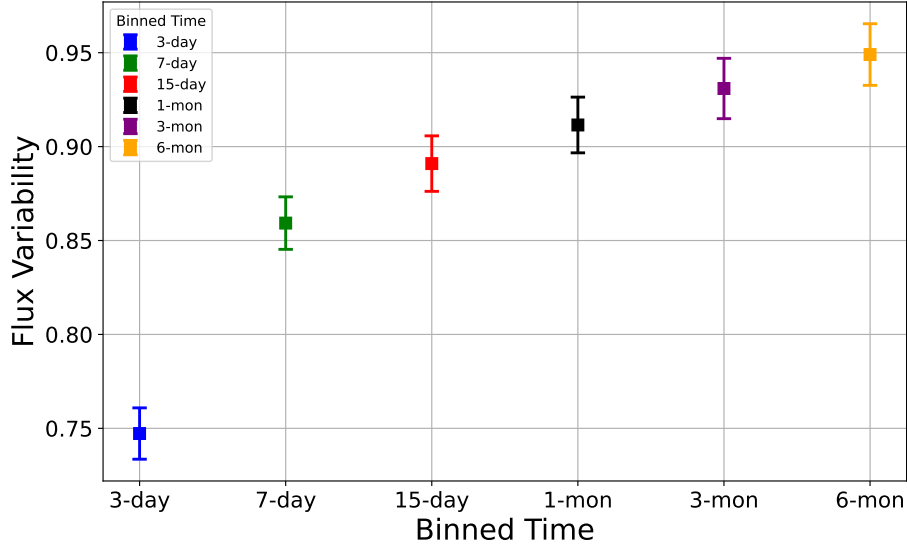


**Figure 6.** Variation of  $F_{var}$  with different time binning of  $\gamma$ -ray light curve.

**Table 3.** The parameters obtained by fitting the integrated  $\gamma$ -ray spectrum of S1, Q1, S2, and S3 states of PKS0805-07 with the PL and LP model. Col. 1: flux state; 2: time period of flux state; 3: fitted model; 4: integrated flux in units of  $10^{-7}$  photons  $\text{cm}^{-2} \text{s}^{-1}$ ; 5: PL index or index defined at pivot energy; 6: curvature parameter; 7: test statistics; 8:  $-\log(\text{likelihood})$ ; 9: significance of curvature.

State	Period	Model	$F_{0.1-300}$	$\Gamma$ or $\alpha$	$\beta$	TS	$-\log \mathcal{L}$	$\text{TS}_{\text{curve}}$
S1	54940-54990	PL	$2.91 \pm 0.18$	$1.90 \pm 0.04$	—	1748	17566	—
		LP	$2.60 \pm 0.21$	$1.8 \pm 0.06$	$0.06 \pm 0.02$	1775	17563	6
Q1	55475-55530	PL	$1.07 \pm 0.12$	$2.17 \pm 0.11$	—	125	13966	—
		LP	$0.74 \pm 0.19$	$2.09 \pm 0.16$	$0.08 \pm 0.08$	130	13966	0
S2	57060-57100	PL	$3.44 \pm 0.23$	$2.04 \pm 0.04$	—	966	12476	—
		LP	$2.81 \pm 0.26$	$1.89 \pm 0.07$	$0.17 \pm 0.04$	1040	12464	24
S3	59880-59930	PL	$5.61 \pm 0.26$	$2.21 \pm 0.03$	—	1813	18370	—
		LP	$5.4 \pm 0.03$	$2.17 \pm 0.04$	$0.14 \pm 0.03$	1855	18357	26

states. In this model, we consider emission originating from a spherical blob with radius  $R$  filled with a relativistic electron distribution,  $n(\gamma)$ . The blob moves along the jet with a bulk Lorentz factor  $\Gamma$  at a small angle  $\theta$  relative to the observer's line of sight. The beaming factor,  $\delta = 1/\Gamma(1 - \beta \cos \theta)$ , amplifies the blazar emission due to relativistic motion. We assume variability is governed by light crossing time scales, determining the emission region size as  $R \sim \delta t_{var}/(1+z)$ . The relativistic electrons, in the presence of magnetic field  $B$  and target photon field, emit radiation through synchrotron and Inverse Compton (IC) processes. We assume seed photons for the IC process are synchrotron photons from the jet itself, resulting in emission through Synchrotron Self-Compton (SSC) process. We express the electron Lorentz factor  $\gamma$  in terms of a new variable  $\xi$  such that

$\xi = \gamma\sqrt{\mathbb{C}}$ , where  $\mathbb{C} = 1.36 \times 10^{-11} \delta B/(1+z)$ . Following Begelman et al. (1984); Dermer (1995); Finke et al. (2008); Sahayanathan et al. (2018), the synchrotron flux at energy  $\epsilon$  can be obtained using the equation

$$F_{\text{syn}}(\epsilon) = \frac{\delta^3(1+z)}{d_L^2} V \mathbb{A} \int_{\xi_{\text{min}}}^{\xi_{\text{max}}} f(\epsilon/\xi^2) n(\xi) d\xi, \quad (10)$$

where  $d_L$  represents the luminosity distance,  $V$  is the emission region volume,  $\mathbb{A} = \frac{\sqrt{3}\pi e^3 B}{16m_e c^2 \sqrt{\mathbb{C}}}$ . The symbols  $\xi_{\text{min}}$  and  $\xi_{\text{max}}$  represent the minimum and maximum energy of electrons, respectively. Additionally, the function  $f(x)$  denotes the synchrotron emissivity function, as described in (Rybicki & Lightman 1986).

The observed SSC flux at energy  $\epsilon$  can be calculated using the following expression [Finke et al. \(2008\)](#); [Sahayanathan et al. \(2018\)](#):

$$F_{\text{SSC}}(\epsilon) = \frac{\delta^3(1+z)}{d_L^2} V_{\mathbb{B}} \epsilon \int_{\xi_{\min}}^{\xi_{\max}} \frac{1}{\xi^2} \int_{x_1}^{x_2} \frac{I_{\text{syn}}(\epsilon_i)}{\epsilon_i^2} f(\epsilon_i, \epsilon, \xi/\sqrt{\mathbb{C}}) d\epsilon_i n(\xi) d\xi \quad (11)$$

where  $\epsilon_i$  corresponds to incident photon energy,  $\mathbb{B} = \frac{3}{4}\sigma_T\sqrt{\mathbb{C}}$ ,  $I_{\text{syn}}(\epsilon_i)$  represents the synchrotron intensity,  $x_1 = \frac{\mathbb{C}\epsilon}{4\xi^2(1-\sqrt{\mathbb{C}}\epsilon/\xi m_e c^2)}$ ,  $x_2 = \frac{\epsilon}{(1-\sqrt{\mathbb{C}}\epsilon/\xi m_e c^2)}$ , and

$$f(\epsilon_i, \epsilon, \xi) = 2q \log q + (1+2q)(1-q) + \frac{\kappa^2 q^2 (1-q)}{2(1+\kappa q)}$$

where  $q = \frac{\mathbb{C}\epsilon}{4\xi^2\epsilon_i(1-\sqrt{\mathbb{C}}\epsilon/\xi m_e c^2)}$  and  $\kappa = \frac{4\xi\epsilon_i}{\sqrt{\mathbb{C}}m_e c^2}$ .

In a similar manner, the observer can determine the observed EC flux through the following equation ([Sahayanathan et al. 2018](#)):

$$F_{\text{EC}}(\epsilon) = \frac{\delta^3(1+z)}{d_L^2} V_{\mathbb{D}} \epsilon \int_0^\infty d\epsilon_i^* \int_{\xi_{\min}}^{\xi_{\max}} d\xi \frac{N(\xi)}{\xi^2} \frac{U_{\text{ph}}^*}{\epsilon_i^*} \eta(\xi, \epsilon_s, \epsilon_i') \quad (12)$$

Where  $\mathbb{D} = \frac{3}{32\pi} c\beta\sigma_T\sqrt{\mathbb{C}}$ ,  $\epsilon_i^*$  represents the energy of target photons in the AGN frame,  $U_{\text{ph}}^*$  signifies the energy density of target photons,

$$\eta(\xi, \epsilon_s, \epsilon_i') = y + \frac{1}{y} + \frac{\mathbb{C}\epsilon_s^2}{\xi^2\epsilon_i'^2 y^2} - \frac{2\nu_s\sqrt{\mathbb{C}}}{\xi\epsilon_i' y} \quad (13)$$

where  $y = 1 - \frac{\sqrt{\mathbb{C}}\epsilon_s}{\xi m_e c^2}$ .

We solved Equations 10, 11 and 12 numerically. for a broken power law electron distribution The resulting numerical code is incorporated as a local convolution model in XSPEC for statistical fitting of broadband SEDs. A systematic error of 5% was added individually to UVOT. The observed broadband spectrum is mainly determined by 10 parameters:  $\xi_b$ ,  $\xi_{\min}$ ,  $\xi_{\max}$ ,  $p$ ,  $q$ ,  $\Gamma$ ,  $B$ ,  $R$ ,  $\theta$ , and norm  $N$ . The code also allows fitting the SED with jet power ( $P_{\text{jet}}$ ) as one of the parameters, with  $N$  fixed. The initial parameter values were selected based on the shape and flux levels of the synchrotron/SSC/EC components during the flaring state. Subsequently, we varied the parameters individually to identify the optimal values. After obtaining the optimal parameter values, we performed the final fit, allowing only four parameters i.e.,

$p$ ,  $q$ ,  $\Gamma$  and  $B$  to vary, while fixing the others, including  $N$ , at their optimal values. The reason for freezing certain parameters is the limited information available in the Optical/UV, X-ray, and  $\gamma$ -ray bands. Moreover, we used the **Tbabs** model to account for absorption in the X-ray spectrum. We observed that the synchrotron, SSC and EC emissions yielded a satisfactory fit for all flux states, resulting in  $\chi^2/dof$  values of 12.43/12, 9.15/12, 21.74/17 and 13.59/15 for S1, Q1, S2 and S3 states respectively. The resulting SED best-fit model, along with observed points, are depicted in Figure 7 and the corresponding optimal parameters are provided in Table 4.

#### 4. SUMMARY AND DISCUSSION

The continuous monitoring of the FSRQ PKS 0805-07 by Fermi-LAT, coupled with simultaneous observations from Swift-XRT/UVOT, has enabled a comprehensive examination of the source's temporal and spectral characteristics. For the first time, a detailed analysis of the source was carried out in this paper. We have designated HOP 8 (MJD 59370–59965) as the “active state” of the source. The average flux in this time period is higher than the average flux between MJD 54684–59370 (see Table 1). The maximum  $\gamma$ -ray flux in the 3-day and 7-day binned light curves was obtained as  $(1.56 \pm 0.16) \times 10^{-6}$  photons  $\text{cm}^{-2} \text{s}^{-1}$  on MJD 59904.5 and  $(1.34 \pm 0.11) \times 10^{-6}$  photons  $\text{cm}^{-2} \text{s}^{-1}$  on MJD 59901.5, respectively. During the “active state”, the  $\gamma$ -ray light curve revealed the presence of multiple flaring components. The 3-day binned  $\gamma$ -ray light curve showed a total of 11 flaring components during the active state (see Figure 3). We noted that while two components are moderately asymmetric and the other three components are asymmetric (see Table 2). The asymmetry observed in the flare profile could be attributed to fluctuations in the strength of the acceleration process. A gradual rise in the asymmetric flare potentially indicates the acceleration of particles to higher energy levels, while a rapid decay may be associated with the swift energy loss of high-energy particles. The 3-day binned  $\gamma$ -ray light curve revealed the shortest flux doubling time scale of  $t_{\text{var}} = 2.80 \pm 0.77$  days. Further, we utilized the Z-transformed discrete correlation function (ZDCF, [Alexander 1997](#)) to find the correlation and possible lag between flux and index in the time interval MJD 59582 to 60112 using a 3-day binned  $\gamma$ -ray light curve. A consistent trend of spectral hardening with increased brightness was observed in the  $\gamma$ -ray light curve. Moreover, we noted that the index lags behind the flux by 121 (+27.2, -3.51) days.

We observed that  $F_{\text{var}}$  increases with larger bin sizes. In our analysis, we applied a  $TS > 4$  threshold to in-

**Table 4.** Broadband SED model parameters of PKS 0805-07 for various flux states. Col. 1: Low energy particle index, 2: High energy particle index, 3: Magnetic field in units of  $10^{-3}$  Gauss, 4: Bulk Lorentz factor of the emission region, 5:  $\chi^2/dof$ , 6: Logarithmic jet power in units of  $\text{erg s}^{-1}$ , 7: Normalization. The size of the emission region ( $R$ ) was fixed at  $10^{17}$  cm,  $\xi_{\max}$  fixed at 10, viewing angle ( $\theta$ ) at  $2^\circ$ , and target photon temperature at 1000 K. The  $\xi_{\min}$  parameter ranges between  $(0.7 - 1.9) \times 10^{-3}$ . The fraction of seed photons undergoing IC scattering ranges from 0.2-0.4 percent. The values in subscript and superscript for parameters in the model represent their lower and upper values, respectively, obtained through the broadband spectral fitting.

State	Free Parameters							
	$\xi_{brk}$	p	q	B	$\Gamma$	$\chi^2/dof$	$P_{jet}$	N
S1	$4.20 \times 10^{-2}$	$2.20_{2.16}^{2.24}$	$5.49_{5.02}^{6.10}$	$0.27_{0.25}^{0.28}$	$22.86_{21.84}^{24.08}$	12.43/12	46.30	$9.18 \times 10^{-10}$
Q1	$3.24 \times 10^{-2}$	$2.66_{2.49}^{2.82}$	$5.58_{4.31}^{6.53}$	$0.18_{0.15}^{0.23}$	$10.15_{8.29}^{11.84}$	9.15/12	45.62	$2.43 \times 10^{-9}$
S2	$3.4 \times 10^{-2}$	$2.34_{2.30}^{2.39}$	$5.52_{5.16}^{5.90}$	$0.20_{0.18}^{0.21}$	$19.71_{18.92}^{20.22}$	21.74/17	46.09	$1.23 \times 10^{-8}$
S3	$2.91 \times 10^{-2}$	$2.76_{2.70}^{2.81}$	$5.47_{5.17}^{5.79}$	$0.26_{0.25}^{0.29}$	$21.66_{21.13}^{22.22}$	13.59/15	46.10	$1.93 \times 10^{-9}$

clude only statistically significant data points. However, it is important to note that excluding data points with  $TS < 4$  for Fermi light curves, which typically have the same exposure in each observation, effectively removes low-flux points. This may introduce a bias in the  $F_{var}$  calculation, as removing these points reduces the variability amplitude. Additionally, in the lower time-binned light curves (e.g., 3-day or 7-day), the fraction of points having  $TS < 4$  are larger compared to higher time binned light curves (e.g., 3 or 6-month). Consequently, more data points are excluded from the 3-day or 7-day binned light curves, resulting in a noticeable decrease in the  $F_{var}$  values, as shown in Figure 6. This contrasts with the trend observed when all measurements are included, where  $F_{var}$  increases with the decrease in size of time bin. As such, the inclusion of all data points, despite their uncertainties, reveals an opposite trend in the time-binned variability (Schleicher et al. 2019).

We examined the flux distribution of the  $\gamma$ -ray light curve using Anderson-Darling (AD) test and histogram fitting. These tests reject the assumption of normality in the flux distribution and instead suggest that the flux distribution follows a lognormal pattern. The observation of a lognormal distribution implies that the underlying emission process responsible for the variability is multiplicative rather than additive (see Shah et al. 2018, and reference therein). For blazars, where the emission mainly originates from the jet, a potential explanation for the observation of lognormal behavior is that the disk fluctuations are imprinted on the jet emission (Giebels

& Degrange 2009; McHardy 2010; Shah et al. 2018). Conversely, the minute timescale variations observed in  $\gamma$ -ray light curves suggest that the jet emission should be independent of accretion disk fluctuations (Narayan & Piran 2012). In such cases, the lognormal distribution in flux can be explained by linear Gaussian perturbations in particle acceleration timescales (Sinha et al. 2018). Alternatively, a log-normal flux distribution can also arise from additive processes under certain conditions. For instance, if the blazar jet is considered as a collection of mini-jets, the logarithm of the composite flux would exhibit a normal distribution (Biteau & Giebels 2012).

The spectral examination of the  $\gamma$ -ray light curve within the specified flux states reveals significant curvature in the S2 (TS curve = 24) and S3 (TS curve = 26) states. The conventional approach to comprehend spectral curvature involves considering radiative losses in the emission region, as proposed by Krawczynski et al. (2002). Alternatively, Massaro et al. (2004) demonstrated that curved features in particle distributions may arise when the acceleration probability is energy-dependent. Another explanation involves the energy dependency of the escape timescale in the acceleration zone, as proposed by Goswami et al. (2018); Hota et al. (2021); Khatoun et al. (2022). Additionally, Hota et al. (2021) demonstrated that models incorporating power-law (PL) with maximum energy, energy-dependent diffusion (EED), and energy-dependent acceleration (EDA) can generate spectral curvature. However, they ruled out the PL with

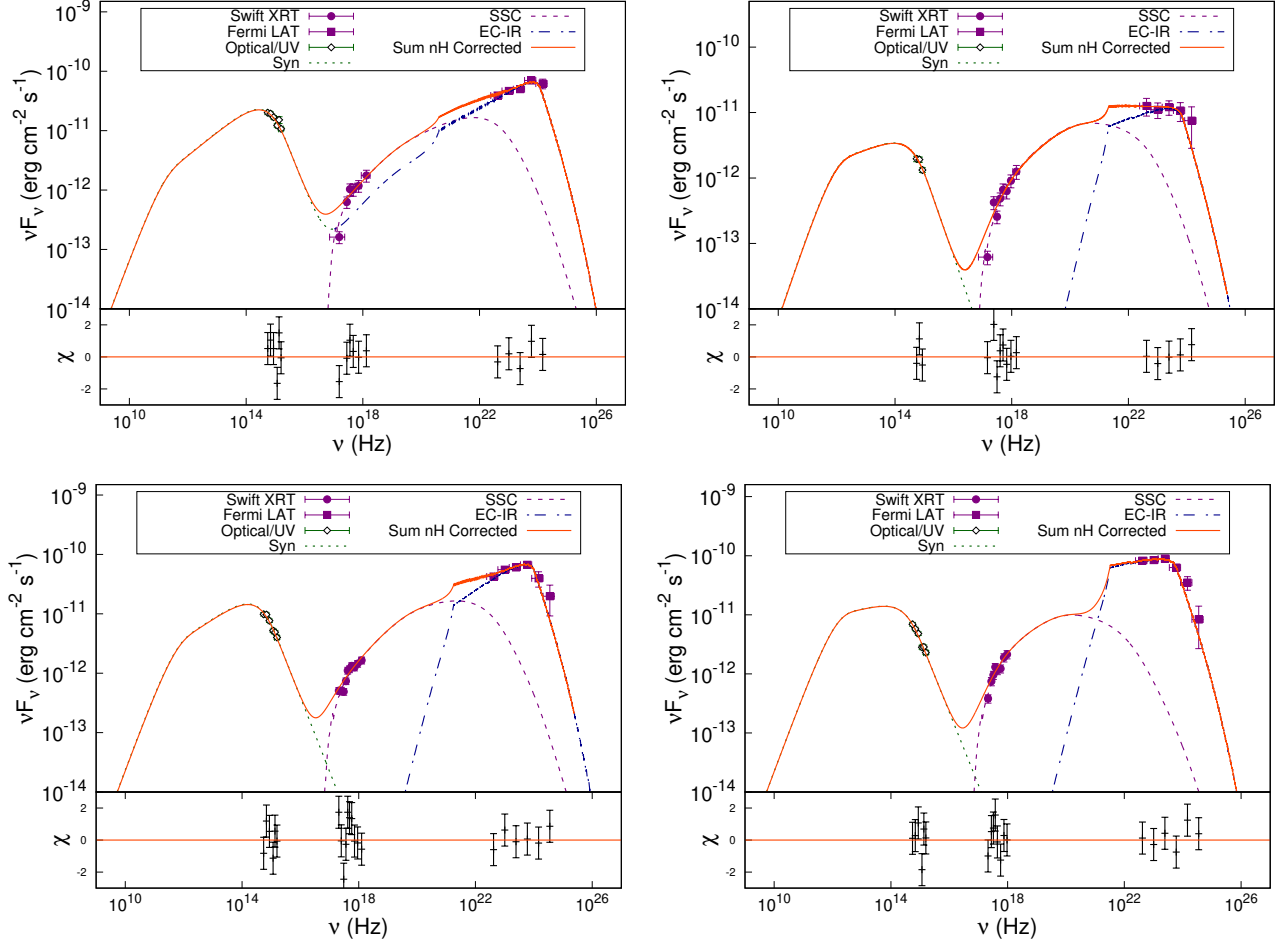


**Figure 7.** The broadband SED of PKS 0805-07 acquired during the flux states S1 (on the top left panel), Q1 (on the top right panel), S2 (on the bottom left panel) and S3 (on the bottom right panel). The flux points denoted by filled diamonds correspond to *Swift*-UVOT, squares correspond to *Swift*-XRT, and filled circles correspond to *Fermi*-LAT. The solid red curve illustrates the combined best-fit synchrotron, SSC, and EC spectra.

maximum energy model due to inconsistencies between observed correlations and model predictions.

In this paper, we employed the one-zone leptonic model to reproduce the broadband spectra of the selected flux states. We assumed the steady-state emission within the chosen flux intervals. Our modeling relied on a BPL electron distribution, extensively utilized for SED modeling in prior research (Sahayanathan et al. 2018; Shah 2024). This BPL electron distribution, subject to synchrotron, SSC, and EC losses, successively reproduces the broad-band emission across all flux intervals. We observed that the EC scattering of IR target photons yielded a satisfactory fit to the data. The statistical fitting process involves treating  $p$ ,  $q$ ,  $\Gamma$ ,  $\xi_{break}$  and  $B$  as free parameters, while the remaining parameters are held constant at typical values specific to the correspond-

ing flux state. The corresponding optimal parameters are detailed in Table 4. It is observed that the magnetic field strength  $B$  varies within the range of  $(0.18 \text{ to } 0.27) \times 10^{-3}$  Gauss, showing an upward trend from low flux state to high flux state. Notably, such low magnetic field values, measured in milligauss, have also been reported in radio observations of FSRQs (e.g. Kim et al. 2022; Jeong et al. 2023).

Similarly, the Lorentz factor  $\Gamma$  ranges from 10.15-22.86, exhibiting an increase from Q1 to S3, with the highest  $\Gamma$  observed in state S1. Furthermore, there exists a positive correlation between  $B$  and  $\Gamma$ . The break energy, defined as  $\xi_{break}$ , ranges between  $(2.91 \text{ to } 4.20) \times 10^{-2}$ . Nevertheless, there is no clear trend observed from the low to high flux states. The derived spectral indices, denoted as  $p$  and  $q$ , vary between 2.20 - 2.76 and 5.47 -



5.58, respectively. These index values suggest a steeper spectral slope beyond the break energy than expected solely from synchrotron cooling, necessitating alternative explanations. The precise cause for this steepened spectrum remains ambiguous. One plausible explanation could involve the presence of an energy-dependent diffusion coefficient. Earlier investigations, such as those by Zirakashvili & Aharonian (2007), have shown that with an energy-dependent diffusion coefficient, the spectral cutoff adopts a sub-exponential or steeper profile at higher energies. Alternatively, Sahayanathan (2008) demonstrated that a two-zone model incorporating a BPL injection into cooling region can lead to a steeper index after the break energy.

1 We sincerely thank the anonymous referee for his  
 2 valuable feedback and suggestions, which have sig-  
 3 nificantly improved the quality of our manuscript.  
 4 SAD is thankful to the MOMA for the MANF fel-  
 5 lowship (No.F.82-27/2019(SA-III)). ZS is supported  
 6 by the Department of Science and Technology,  
 7 Govt. of India, under the INSPIRE Faculty grant  
 8 (DST/INSPIRE/04/2020/002319). SAD, ZS and NI ex-  
 9 press gratitude to the Inter-University Centre for As-  
 10 tronomy and Astrophysics (IUCAA) in Pune, India, for  
 11 the support and facilities provided.

## REFERENCES

- Abdo, A. A., Ackermann, M., Ajello, M., et al. 2010a, *ApJS*, 188, 405, doi: [10.1088/0067-0049/188/2/405](https://doi.org/10.1088/0067-0049/188/2/405)
- . 2010b, *ApJ*, 722, 520, doi: [10.1088/0004-637X/722/1/520](https://doi.org/10.1088/0004-637X/722/1/520)
- Abdollahi, S., Acero, F., Ackermann, M., et al. 2020, *ApJS*, 247, 33, doi: [10.3847/1538-4365/ab6bcb](https://doi.org/10.3847/1538-4365/ab6bcb)
- Abdollahi, S., Acero, F., Baldini, L., et al. 2022, *ApJS*, 260, 53, doi: [10.3847/1538-4365/ac6751](https://doi.org/10.3847/1538-4365/ac6751)
- Ackermann, M., Anantua, R., Asano, K., et al. 2016, *ApJL*, 824, L20, doi: [10.3847/2041-8205/824/2/L20](https://doi.org/10.3847/2041-8205/824/2/L20)
- Aharonian, F., Akhperjanian, A. G., Bazer-Bachi, A. R., et al. 2007, *ApJL*, 664, L71, doi: [10.1086/520635](https://doi.org/10.1086/520635)
- Alexander, T. 1997, in *Astrophysics and Space Science Library*, Vol. 218, *Astronomical Time Series*, ed. D. Maoz, A. Sternberg, & E. M. Leibowitz, 163, doi: [10.1007/978-94-015-8941-3\\_14](https://doi.org/10.1007/978-94-015-8941-3_14)
- Ansoldi, S., Antonelli, L. A., Arcaro, C., et al. 2018, *ApJL*, 863, L10, doi: [10.3847/2041-8213/aad083](https://doi.org/10.3847/2041-8213/aad083)
- Arnaud, K. A. 1996, in *Astronomical Society of the Pacific Conference Series*, Vol. 101, *Astronomical Data Analysis Software and Systems V*, ed. G. H. Jacoby & J. Barnes, 17
- Atwood, W. B., Abdo, A. A., Ackermann, M., et al. 2009, *ApJ*, 697, 1071, doi: [10.1088/0004-637X/697/2/1071](https://doi.org/10.1088/0004-637X/697/2/1071)
- Begelman, M. C., Blandford, R. D., & Rees, M. J. 1984, *Reviews of Modern Physics*, 56, 255, doi: [10.1103/RevModPhys.56.255](https://doi.org/10.1103/RevModPhys.56.255)
- Biteau, J., & Giebels, B. 2012, *A&A*, 548, A123, doi: [10.1051/0004-6361/201220056](https://doi.org/10.1051/0004-6361/201220056)
- Błażejowski, M., Sikora, M., Moderski, R., & Madejski, G. M. 2000, *ApJ*, 545, 107, doi: [10.1086/317791](https://doi.org/10.1086/317791)
- Böttcher, M., Reimer, A., Sweeney, K., & Prakash, A. 2013, *ApJ*, 768, 54, doi: [10.1088/0004-637X/768/1/54](https://doi.org/10.1088/0004-637X/768/1/54)
- Breeveld, A. A., Curran, P. A., Hoversten, E. A., et al. 2010, *MNRAS*, 406, 1687, doi: [10.1111/j.1365-2966.2010.16832.x](https://doi.org/10.1111/j.1365-2966.2010.16832.x)
- Bulgarelli, A., Di Piano, A., Pittori, C., et al. 2022, *The Astronomer’s Telegram*, 15768, 1

- Ciprini, S. 2009a, *The Astronomer's Telegram*, 2136, 1  
 —. 2009b, *The Astronomer's Telegram*, 2048, 1
- Dermer, C. D. 1995, *ApJL*, 446, L63, doi: [10.1086/187931](https://doi.org/10.1086/187931)
- Dermer, C. D., Schlickeiser, R., & Mastichiadis, A. 1992, *A&A*, 256, L27
- Di Gesu, L., Donnarumma, I., Tavecchio, F., et al. 2022, *ApJL*, 938, L7, doi: [10.3847/2041-8213/ac913a](https://doi.org/10.3847/2041-8213/ac913a)
- Edwards, P. G., Stevens, J., Kadler, M., et al. 2022, *The Astronomer's Telegram*, 15692, 1
- Eisenstein, D. J., & Hut, P. 1998, *ApJ*, 498, 137, doi: [10.1086/305535](https://doi.org/10.1086/305535)
- Fan, J. H., Xu, W., Pan, J., & Yuan, Y. H. 2011, in *Jets at All Scales*, ed. G. E. Romero, R. A. Sunyaev, & T. Belloni, Vol. 275, 164–167, doi: [10.1017/S1743921310015875](https://doi.org/10.1017/S1743921310015875)
- Fan, J. H., Kurtanidze, S. O., Liu, Y., et al. 2021, *The Astrophysical Journal Supplement Series*, 253, 10, doi: [10.3847/1538-4365/abd32d](https://doi.org/10.3847/1538-4365/abd32d)
- Finke, J. D., Dermer, C. D., & Böttcher, M. 2008, *ApJ*, 686, 181, doi: [10.1086/590900](https://doi.org/10.1086/590900)
- Fitzpatrick, E. L., & Massa, D. 2007, *ApJ*, 663, 320, doi: [10.1086/518158](https://doi.org/10.1086/518158)
- Foschini, L., Ghisellini, G., Tavecchio, F., Bonnoli, G., & Stamerra, A. 2011, *A&A*, 530, A77, doi: [10.1051/0004-6361/201117064](https://doi.org/10.1051/0004-6361/201117064)
- Gasparyan, S., Bégué, D., & Sahakyan, N. 2022, *MNRAS*, 509, 2102, doi: [10.1093/mnras/stab2688](https://doi.org/10.1093/mnras/stab2688)
- Gehrels, N., Chincarini, G., Giommi, P., et al. 2004, *ApJ*, 611, 1005, doi: [10.1086/422091](https://doi.org/10.1086/422091)
- Ghisellini, G., Padovani, P., Celotti, A., & Maraschi, L. 1993, *ApJ*, 407, 65, doi: [10.1086/172493](https://doi.org/10.1086/172493)
- Giebels, B., & Degrange, B. 2009, *A&A*, 503, 797, doi: [10.1051/0004-6361/200912303](https://doi.org/10.1051/0004-6361/200912303)
- Goswami, P., Sahayanathan, S., Sinha, A., Misra, R., & Gogoi, R. 2018, *MNRAS*, 480, 2046, doi: [10.1093/mnras/sty2003](https://doi.org/10.1093/mnras/sty2003)
- Hota, J., Shah, Z., Khatoon, R., et al. 2021, *MNRAS*, 508, 5921, doi: [10.1093/mnras/stab2903](https://doi.org/10.1093/mnras/stab2903)
- IceCube Collaboration, Aartsen, M. G., Ackermann, M., et al. 2018, *Science*, 361, eaat1378, doi: [10.1126/science.aat1378](https://doi.org/10.1126/science.aat1378)
- Jeong, H.-W., Lee, S.-S., Cheong, W. Y., et al. 2023, *MNRAS*, 523, 5703, doi: [10.1093/mnras/stad1736](https://doi.org/10.1093/mnras/stad1736)
- Jones, T. W., O'Dell, S. L., & Stein, W. A. 1974, *ApJ*, 188, 353, doi: [10.1086/152724](https://doi.org/10.1086/152724)
- Jorstad, S. G., Marscher, A. P., Raiteri, C. M., et al. 2022, *Nature*, 609, 265, doi: [10.1038/s41586-022-05038-9](https://doi.org/10.1038/s41586-022-05038-9)
- Kalberla, P. M. W., Burton, W. B., Hartmann, D., et al. 2005, *A&A*, 440, 775, doi: [10.1051/0004-6361:20041864](https://doi.org/10.1051/0004-6361:20041864)
- Keivani, A., Murase, K., Petropoulou, M., et al. 2018, *ApJ*, 864, 84, doi: [10.3847/1538-4357/aad59a](https://doi.org/10.3847/1538-4357/aad59a)
- Khatoon, R., Shah, Z., Hota, J., et al. 2022, *MNRAS*, 515, 3749, doi: [10.1093/mnras/stac1964](https://doi.org/10.1093/mnras/stac1964)
- Kim, S.-H., Lee, S.-S., Lee, J. W., et al. 2022, *MNRAS*, 510, 815, doi: [10.1093/mnras/stab3473](https://doi.org/10.1093/mnras/stab3473)
- Krawczynski, H., Coppi, P. S., & Aharonian, F. 2002, *MNRAS*, 336, 721, doi: [10.1046/j.1365-8711.2002.05750.x](https://doi.org/10.1046/j.1365-8711.2002.05750.x)
- La Mura, G. 2022, *The Astronomer's Telegram*, 15676, 1
- Lister, M. L., Homan, D. C., Hovatta, T., et al. 2019, *ApJ*, 874, 43, doi: [10.3847/1538-4357/ab08ee](https://doi.org/10.3847/1538-4357/ab08ee)
- Mannheim, K. 1993, *A&A*, 269, 67, doi: [10.48550/arXiv.astro-ph/9302006](https://doi.org/10.48550/arXiv.astro-ph/9302006)
- Maraschi, L., Ghisellini, G., & Celotti, A. 1992, *ApJL*, 397, L5, doi: [10.1086/186531](https://doi.org/10.1086/186531)
- Massaro, E., Perri, M., Giommi, P., Nesci, R., & Verrecchia, F. 2004, *A&A*, 422, 103, doi: [10.1051/0004-6361:20047148](https://doi.org/10.1051/0004-6361:20047148)
- McHardy, I. 2010, in *Lecture Notes in Physics*, Berlin Springer Verlag, ed. T. Belloni, Vol. 794, 203, doi: [10.1007/978-3-540-76937-8\\_8](https://doi.org/10.1007/978-3-540-76937-8_8)
- Meyer, M., Scargle, J. D., & Blandford, R. D. 2019, *ApJ*, 877, 39, doi: [10.3847/1538-4357/ab1651](https://doi.org/10.3847/1538-4357/ab1651)
- Mücke, A., & Protheroe, R. J. 2001, *Astroparticle Physics*, 15, 121, doi: [10.1016/S0927-6505\(00\)00141-9](https://doi.org/10.1016/S0927-6505(00)00141-9)
- Mücke, A., Protheroe, R. J., Engel, R., Rachen, J. P., & Stanev, T. 2003, *Astroparticle Physics*, 18, 593, doi: [10.1016/S0927-6505\(02\)00185-8](https://doi.org/10.1016/S0927-6505(02)00185-8)
- Narayan, R., & Piran, T. 2012, *MNRAS*, 420, 604, doi: [10.1111/j.1365-2966.2011.20069.x](https://doi.org/10.1111/j.1365-2966.2011.20069.x)
- Nolan, P. L., Abdo, A. A., Ackermann, M., et al. 2012, *ApJS*, 199, 31, doi: [10.1088/0067-0049/199/2/31](https://doi.org/10.1088/0067-0049/199/2/31)
- Poole, T. S., Breeveld, A. A., Page, M. J., et al. 2008, *MNRAS*, 383, 627, doi: [10.1111/j.1365-2966.2007.12563.x](https://doi.org/10.1111/j.1365-2966.2007.12563.x)
- Prokhorov, D. A., & Moraghan, A. 2017, *MNRAS*, 471, 3036, doi: [10.1093/mnras/stx1742](https://doi.org/10.1093/mnras/stx1742)
- Qian, S. J. 2023, *arXiv e-prints*, arXiv:2306.06863, doi: [10.48550/arXiv.2306.06863](https://doi.org/10.48550/arXiv.2306.06863)
- Roming, P. W. A., Kennedy, T. E., Mason, K. O., et al. 2005, *SSRv*, 120, 95, doi: [10.1007/s11214-005-5095-4](https://doi.org/10.1007/s11214-005-5095-4)
- Rybicki, G. B., & Lightman, A. P. 1986, *Radiative Processes in Astrophysics*
- Sahakyan, N. 2018, *ApJ*, 866, 109, doi: [10.3847/1538-4357/aadade](https://doi.org/10.3847/1538-4357/aadade)
- Sahayanathan, S. 2008, *MNRAS*, 388, L49, doi: [10.1111/j.1745-3933.2008.00497.x](https://doi.org/10.1111/j.1745-3933.2008.00497.x)
- Sahayanathan, S., Sinha, A., & Misra, R. 2018, *Research in Astronomy and Astrophysics*, 18, 035, doi: [10.1088/1674-4527/18/3/35](https://doi.org/10.1088/1674-4527/18/3/35)
- Scargle, J. D., Norris, J. P., Jackson, B., & Chiang, J. 2013, *ApJ*, 764, 167, doi: [10.1088/0004-637X/764/2/167](https://doi.org/10.1088/0004-637X/764/2/167)

- Schleicher, B., Arbet-Engels, A., Baack, D., et al. 2019, *Galaxies*, 7, 62, doi: [10.3390/galaxies7020062](https://doi.org/10.3390/galaxies7020062)
- Shah, Z. 2024, *MNRAS*, 527, 5140, doi: [10.1093/mnras/stad3534](https://doi.org/10.1093/mnras/stad3534)
- Shah, Z., Jithesh, V., Sahayanathan, S., Misra, R., & Iqbal, N. 2019, *MNRAS*, 484, 3168, doi: [10.1093/mnras/stz151](https://doi.org/10.1093/mnras/stz151)
- Shah, Z., Mankuzhiyil, N., Sinha, A., et al. 2018, *Research in Astronomy and Astrophysics*, 18, 141, doi: [10.1088/1674-4527/18/11/141](https://doi.org/10.1088/1674-4527/18/11/141)
- Shah, Z., Sahayanathan, S., Mankuzhiyil, N., et al. 2017, *MNRAS*, 470, 3283, doi: [10.1093/mnras/stx1194](https://doi.org/10.1093/mnras/stx1194)
- Sikora, M., Begelman, M. C., & Rees, M. J. 1994, *ApJ*, 421, 153, doi: [10.1086/173633](https://doi.org/10.1086/173633)
- Sinha, A., Khatoon, R., Misra, R., et al. 2018, *MNRAS*, 480, L116, doi: [10.1093/mnrasl/sly136](https://doi.org/10.1093/mnrasl/sly136)
- Tripathi, T., Gupta, A. C., Takey, A., et al. 2023, *Monthly Notices of the Royal Astronomical Society*, 527, 5220, doi: [10.1093/mnras/stad3574](https://doi.org/10.1093/mnras/stad3574)
- Urry, C. M., & Padovani, P. 1995, *PASP*, 107, 803, doi: [10.1086/133630](https://doi.org/10.1086/133630)
- Vaughan, S., Edelson, R., Warwick, R. S., & Uttley, P. 2003, *MNRAS*, 345, 1271, doi: [10.1046/j.1365-2966.2003.07042.x](https://doi.org/10.1046/j.1365-2966.2003.07042.x)
- Villata, M., Raiteri, C. M., Balonek, T. J., et al. 2006, *A&A*, 453, 817, doi: [10.1051/0004-6361:20064817](https://doi.org/10.1051/0004-6361:20064817)
- White, G. L., Jauncey, D. L., Savage, A., et al. 1988, *ApJ*, 327, 561, doi: [10.1086/166216](https://doi.org/10.1086/166216)
- Wood, M., Caputo, R., Charles, E., et al. 2017, in *International Cosmic Ray Conference*, Vol. 301, 35th International Cosmic Ray Conference (ICRC2017), 824, doi: [10.22323/1.301.0824](https://doi.org/10.22323/1.301.0824)
- Xiao, H., Ouyang, Z., Zhang, L., et al. 2022, *The Astrophysical Journal*, 925, 40, doi: [10.3847/1538-4357/ac36da](https://doi.org/10.3847/1538-4357/ac36da)
- Zirakashvili, V. N., & Aharonian, F. 2007, *A&A*, 465, 695, doi: [10.1051/0004-6361:20066494](https://doi.org/10.1051/0004-6361:20066494)